1- SUPPLEMENTAL FIGURES

Figure S1, related to Figure 2

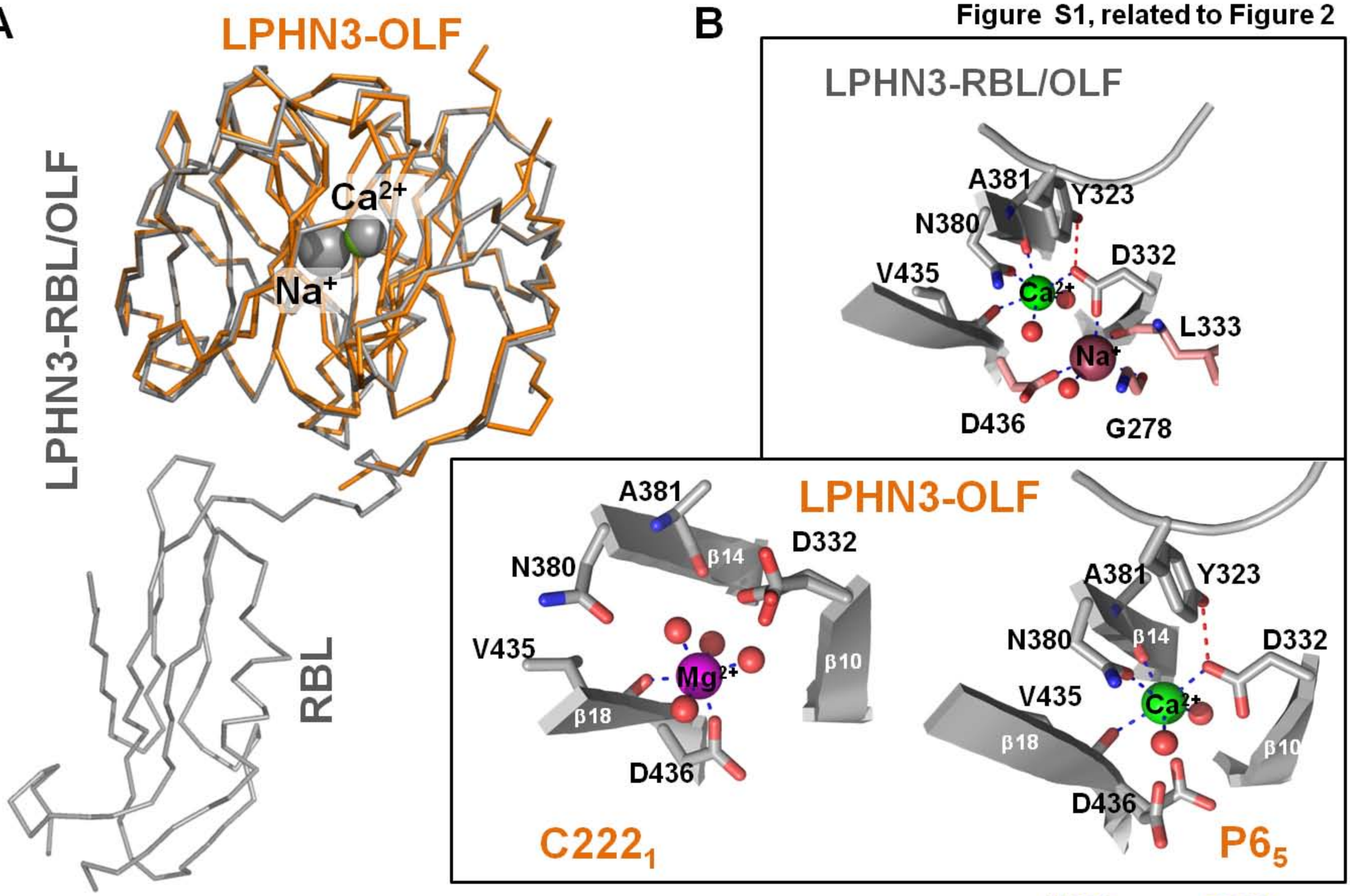

Supplemental Figure S1 - Comparison between LPHN3-OLF and the structurally available OLF domains. (A), overlay of LPHN3-OLF structure (orange) with the published LPHN3-RBL/OLF (gray, Jackson et al., 2015) indicating the relative orientation of the RBL domain. **(B),** Comparative analysis of the metal binding pocket of LPHN3-RBL/OLF with our two crystal forms. **(C),** Overlay of LPHN3-OLF (orange) with myocilin-OLF (PDB ID: 4WXQ, Donegan et al., 2014), with central-pore ions represented as spheres. The identity and coordination states of myocilin-OLF ions are similar as in LPHN3-RBL/OLFs showed in **(A-B)**. **(D),** Comparison of LPHN3-OLF (orange) with gliomedin-OLF (gray, Han and Kursula, 2015). Top panel, sequence alignment of the LPHN3-OLF 316-329 with the homologous gliomedin fragment with an indication (arrows) of Y323 and D332 involved in the Ca^{2+} binding and their structurally equivalent F415 and N423 in gliomedin (bottom-right panel). Bottom-left panel, overall overlay of the two OLF domains, showing the central pore Ca^{2+} or Na^{+} ions. Bottom-right panel: zoomed view of the central pore ions and the LPHN3-OLF loop 316-329 (blue) in the two superimposed OLF domain structures to highlight structural similarities.

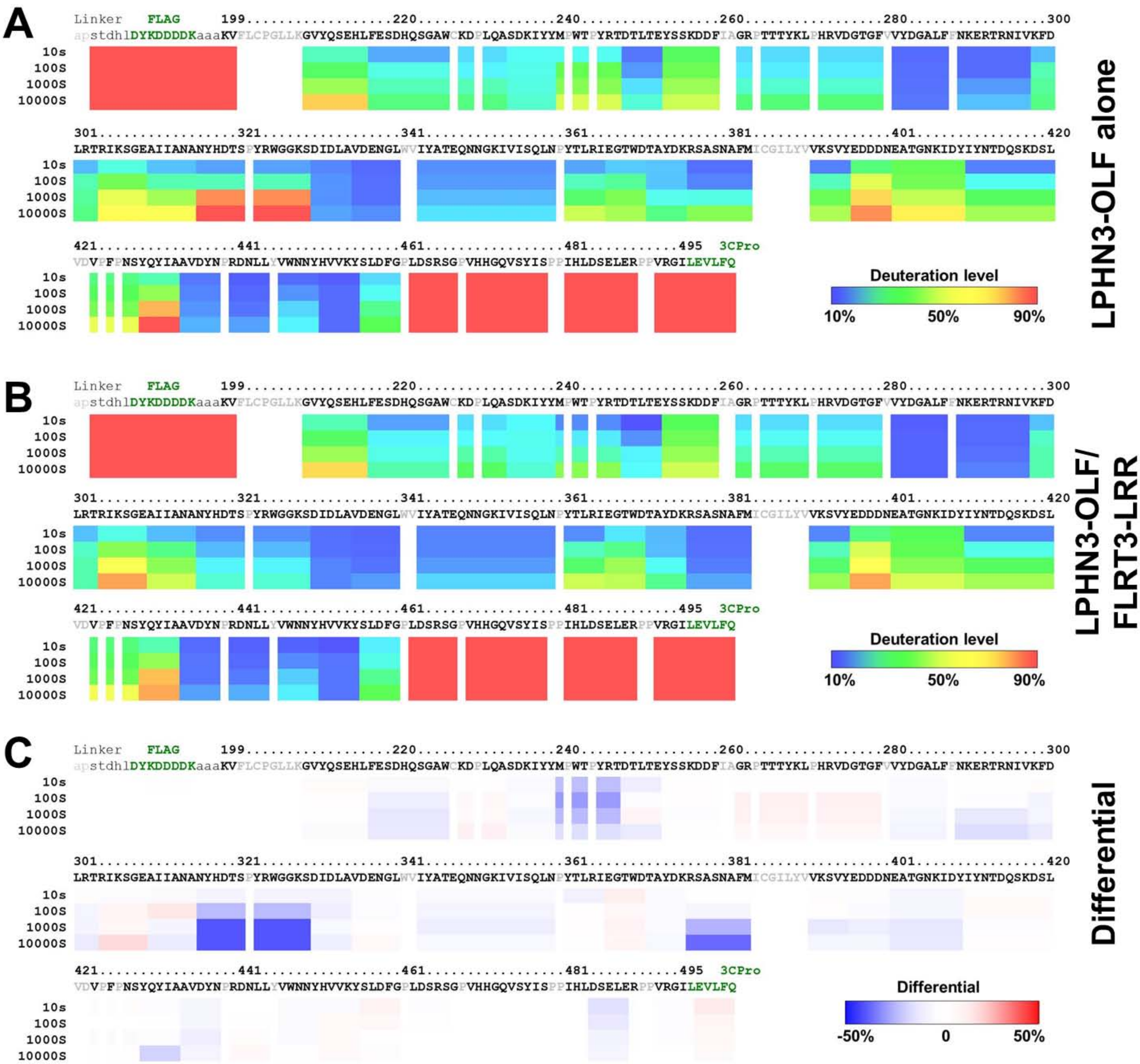

Supplemental Figure S2 - DXMS analysis profiles of LPHN3-OLF, alone or bound to FLRT-LRR domain – (A), Deuteration levels of LPHN3-OLF domain alone. **(B),** Deuteration level of LPHN3-OLF in complex with FLRT3-LRR. **(C),** difference in deuteration level between the free and bound LPHN3-OLF domain. Each fragment is labelled and color coded with the appropriate residues. The percentages of deuteration levels of each peptide fragment at various time points are shown as a heat map color-coded from *blue* (10%) to *red* (90%), as indicated at the bottom of each map. Each block under the protein sequence represents a peptide segment analyzed at each of the four time points (from *top* to *bottom*: 10, 100, 1,000, and 10,000s). Differential deuteration is shown in a color-coded map ranging from blue (−50%) to red (+50%), as indicated at the bottom of the panel. Proline residues and regions with no amide hydrogen exchange data available are colored in *gray*.

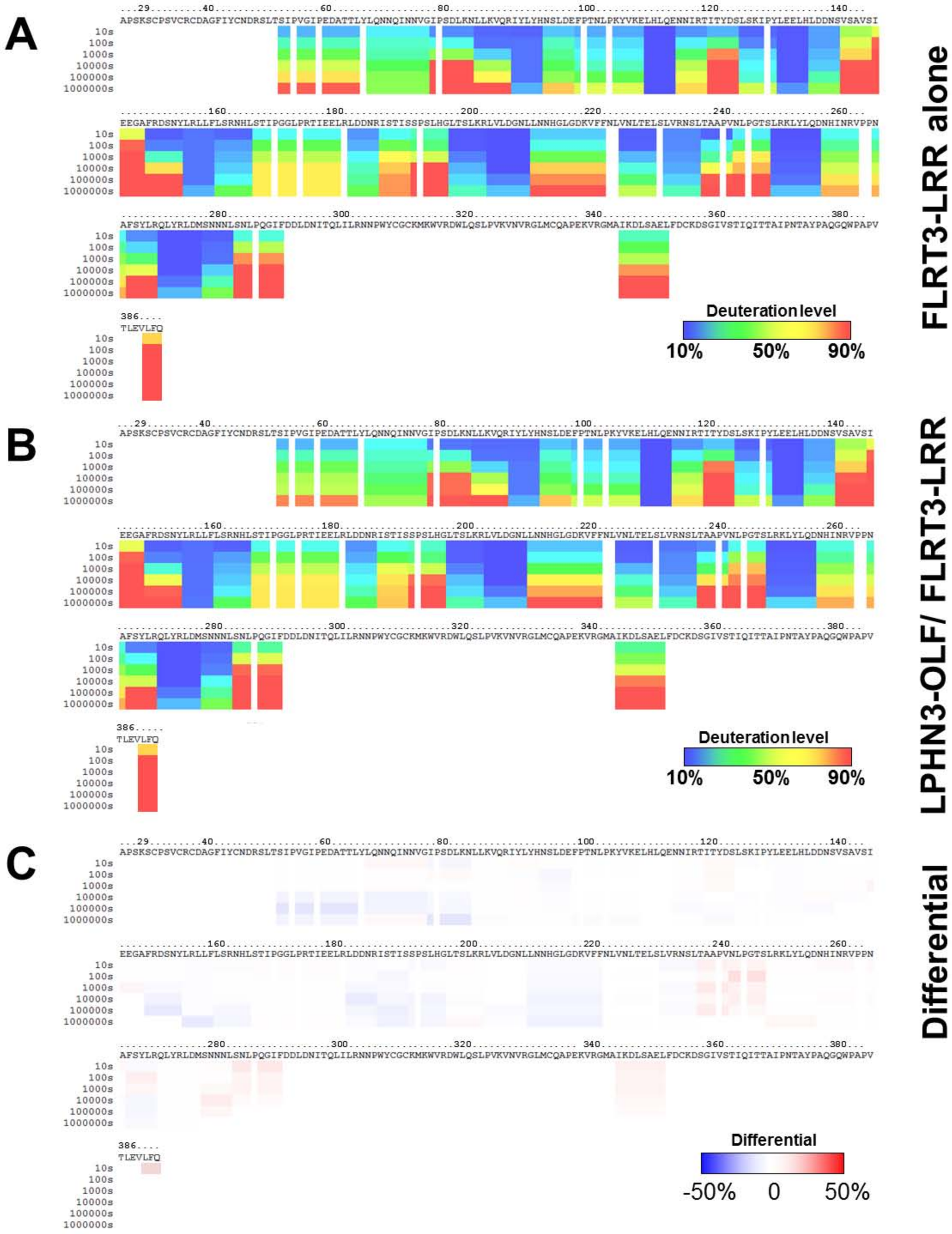

Supplemental Figure S3 - DXMS analysis profiles of FLRT3-LRR, alone or bound to LPHN3-OLF domain – (A), deuteration levels of FLRT3-LRR domain alone. **(B),** Deuteration levels of FLRT3-LRR in complex with LPHN3-OLF. **(C),** Differential deuteration level of FLRT3-LRR in complex with LPHN3-OLF. Each fragment is labelled and color coded with the appropriate residues. The percentages of deuteration levels of each peptide fragment at various time points are shown as a heat map color-coded from *blue* (10%) to *red* (90%), as indicated at the bottom of each map. Each block under the protein sequence represents a peptide segment analyzed at each of the four time points (from *top* to *bottom*: 10, to 1,000,000s). Differential deuteration is shown in a color-coded map ranging from blue (–50%) to red (+50%), as indicated at the bottom of the panel. Proline residues and regions with no amide hydrogen exchange data available are colored in *gray*.
Note that for FLRT3-LRR the deuteration levels before and after complex formation was almost unchanged and larger fragments of the protein were not covered by MS due to posttranslational modification (disulfide bonding and N-linked glycosylation). Although we extended the experiment to 1,000,000s (~11 days), little difference between FLRT3-LRR alone, and in complex with LPHN3-OLF were visible (Supplementary Figure 3). As our crystallographic study show that the interfacing residues are in the concave face of FLRT3-LRR (see below), it is likely that the involvement of the peptide hydrogens in the b-sheet that form this side make them unavailable for deuterium exchange.

2- SUPPLEMENTAL TABLES

Table S1, related to Figure 2: List of fragments that are not resolved by protein crystallography

N-terminal	**leader peptide-**apstdhldykddddkaaaK***-199**
Loop	**395-**(YE)DDDNEAT**-403**
C-terminal	**462-**LDSRSGPVHHGQVSYISPPIHLDSELERPPVRGIlevlfq**-3CPro**

- Upper case, amino acids belonging to LPHN3-OLF, lower case, amino acids remaining after purification (linker, FLAG, 3CPro recognition sequence)

Table S2, related to Figure 2: Structural comparison between LPHN3-OLF ($P6_5$) and other OLF domain structures.

Protein-OLF (PDB ID)	r.m.s.d. (aligned Cα)	% identity
LPHN3-RBL/OLF (5AFB)	0.5 Å (248)	100
Gliomedin-OLF (4D77)	1.4 Å (236)	37
Myocilin-OLF (4WXQ)	1.2 Å (248)	25
Noelin-OLF (5AMO)	1.1 Å (233)	44

Table S3, related to Figure 4: Residues involved in the LPHN3-OLF/FLRT3-LRR complex interface (analysis made with PDBePISA)

Interfacing residues			
LPHN3-OLF residues (Buried area %)		**FLRT3-LRR residues (Buried area %)**	
P244 (10)	N316 (80)	R36 (20)	E132 (50)
Y245 (90)	Y317 (90)	C37 (10)	H134 (100)
T247 (50)	H318 (100)	D38 (30)	D136 (70)
A261 (10)	D319 (70)	F41 (50)	D137 (20)
R263 (20)	T320 (100)	Y43 (100)	L158 (60)
P264 (20)	S321 (20)	N45 (90)	F160 (80)
T265 (10)	K328 (30)	D46 (40)	S162 (20)
T266 (50)	E347 (70)	R47 (30)	E179 (40)
T267 (20)	N350 (70)	Y64 (100)	R181 (80)
R273 (50)	G351 (40)	Q66 (90)	D183 (70)
R292 (80)	D374 (30)	N67 (40)	R203 (60)
T293 (10)	R376 (70)	R87 (20)	V205 (10)
R294 (50)		Y89 (100)	E229 (30)
		Y91 (100)	R275 (20)
		H92 (20)	Q299 (10)
		E108 (20)	K326 (20)
		H110 (100)	N328 (20)
		Q112 (100)	R330 (20)
		E113 (20)	

Hydrogen bonds / Salt bridges		
LPHN3-OLF residues	FLRT3-LRR residues	Distance (Å)
Y245 (OH)	E108 (OE1)	3.4
R273 (NH2)	D183 (OD2)	3.7
R294 (NH2)	D46 (OD2)	2.7
N350 (ND2)	R36 (O)	3.3
R376 (NH1)	Y43 (OH)	2.7
R376 (NH2)	Y64 (OH)	2.8
Y245 (O)	R181 (NH2)	2.8
N316 (OD1)	N45 (ND2)	2.7
Y317 (OH)	N67 (ND2)	2.8
Y317 (O)	Y91 (OH)	3.1
D319 (O)	Y64 (OH)	3.0
T320 (OG1)	Q66 (NE2)	2.9

3- SUPPLEMENTAL PROCEDURE

Cloning of FLRT3 and LPHN3 - The different constructs of LPHN3 and FLRT3 were cloned into a modified pCMV6-XL4 plasmid as previously described (O'Sullivan et al., 2012). A 3C protease cleavage site (LEVLFQ/GP) was introduced between the last residue of the protein of interest and the beginning of the human F_c sequence for purification purpose. All mutations were obtained by using the QuikChange Mutagenesis Kit (Agilent Technology, Santa Clara, CA) and were verified by DNA sequencing.

Cell culture and transfection - HEK293S GnTI- cells were obtained from American Type Culture Collection (ATCC CRL-3022). These cells lack N-acetylglucosaminyltransferaseI (GnTI) activity, and consequently glycosylation remains restricted to a homogeneous seven-residue oligosaccharide (Reeves et al., 2002), thus simplifying structure-function analyses. For the mutational analysis of the interface, regular HEK293 were used instead of GnTI- to ensure a high sugar motives incorporation on the FLRT3-LRR designed N-glycosylation sites. These cells were grown in Dulbecco's Modified Eagle Medium (DMEM) supplemented with 2mM glutamine, 10% FBS, maintained in a humidified incubator at 5% CO2 and 95% air. Stable cells lines were made for each construct and kept in DMEM/10% FBS supplemented with 500 µg/ml of G418 (Geneticin, Sigma) (Comoletti et al., 2003).

Expression and purification of LPHN3 – Proteins were expressed as soluble entities in the cell culture medium of HEK293 cells. The stable cell lines expressing the OLF domain of LPHN3 and the LRR domain of FLRT3 protein were maintained at 37°C and 5% CO2 in DMEM containing up to 2% fetal bovine serum. Proteins were affinity purified using Protein-A Sepharose 4 fast flow resin (GE Healthcare), washed extensively with 50mM Tris HCl pH 7.4

and 450mM NaCl (WASHING buffer), equilibrated with 50mM Tris HCl pH 7.4 and 150mM NaCl (TN buffer) and subsequently cleaved with 3C protease in 50mM Tris HCl pH 7.4 and 150mM NaCl, and 1mM DTT (TND buffer) to elute the protein while removing the IgG fragment. Eluted protein was concentrated to 5mL with Vivaspin concentrators (Sartorius-Stedim) and further purified by size exclusion chromatography as detailed below. The crystallized FLRT3-LRR protein underwent further de-glycosylation by an overnight incubation with a GST-tagged Endoglycosidase F1 (EndoF1) in a 1:20 (w:w) ratio, at 4°C. EndoF1 was subsequently removed on a GSTrap^{TM} FF column (GE Healthcare).

Isothermal titration calorimetry experiments – The purified extracellular domain of both FLRT3 and LPHN3 and their deletion constructs were buffer exchanged by size exclusion chromatography in TN buffer. ITC experiments were carried out on a MicroCal *iTC200* system. Concentrated samples were diluted and degassed before the experiment at the concentrations reported in the figure legends. Either FLRT3 or LPHN3 (10 μM) domains were placed in the MicroCal sample cell and matching buffer was placed in the reference cell. The protein solution in the syringe (100 μM) was added to the cell in a series of multiple injections of varying injection volumes (1 to 1.5μL) at 25°C. The raw ITC data was processed and fitted using a single site model using the ORIGIN software provided by MicroCal and the stoichiometry was not constrained during the model fitting. Blank experiments where concentrated protein was injected in the cell containing buffer alone were performed and subtracted from the positive data.

Analytical ultracentrifugation, sedimentation velocity (SV) - Two loading concentrations of LPHN3-OLF (4.3 μM and 13.2 μM), FLRT3-LRR (7.6 and 18.3 μM), and LPHN3-OLF/FLRT3-LRR (2.9μM and 8.8μM) were measured by SV to monitor the possibility of reversible self-

association. The experiments were performed in a Beckman Optima XL-I analytical ultracentrifuge at the Center for Analytical Ultracentrifugation of Macromolecular Assemblies at the University of Texas Health Science Center at San Antonio. Experimental data were collected at 20°C using 1.2 cm epon 2-channel centerpieces (Beckman-Coulter), using an An60Ti rotor. Hydrodynamic corrections for buffer density and viscosity were estimated by UltraScan to be 1.00603 g/ml and 1.02637 respectively. The partial specific volume was estimated by UltraScan from protein sequence analogous to methods outlined in Laue et al. (Laue et al., 1992) and found to be 0.7259 mL/g.

AUC d*ata analysis:* Sedimentation and diffusion transport in the ultracentrifugation cell is described by the Lamm equation, which can be solved using adaptive finite element methods (Cao and Demeler, 2005, 2008). Whole boundary data obtained in SV experiments are fitted by linear combinations of such solutions using advanced optimization routines (Brookes et al., 2010; Gorbet et al., 2014) that are typically implemented on a supercomputer (Brookes and Demeler, 2008). SV data were analyzed according to method described in (Demeler, 2010). Optimization was performed by 2-dimensional spectrum analysis (2DSA) (Brookes et al., 2010) with simultaneous removal of time- and radially-invariant noise contributions (Schuck and Demeler, 1999). Diffusion-corrected integral sedimentation coefficient distributions were obtained from the enhanced van Holde – Weischet analysis (Demeler and van Holde, 2004). Molecular weights and frictional ratios were determined with the parametrically constrained spectrum analysis (PCSA) (Gorbet et al., 2014). The 2DSA calculations are computationally intensive and are carried out on high-performance computing platforms (Brookes and Demeler, 2008). A reversibly self-associating monomer-dimer model was fitted to the sedimentation velocity data using the genetic algorithm-Monte Carlo analysis. During the fit the known molecular weight (which included the three N-linked glycosylation sites), was fixed, and the partial specific volume, frictional ratios, KD and koff rate were floated. All calculations were

performed on the Stampede and Lonestar cluster at the Texas Advanced Computing Center at the University of Texas at Austin.

Crystallization and diffraction data collection – Prior to crystallization, the affinity-column purified LPHN3-OLF and FLRT3-LRR were fractionated by size exclusion chromatography using a Superdex 200 16/600 (GE Healthcare) in 50mM Tris-HCl, pH 7.4, and 150mM NaCl. The collected fractions were concentrated to 10-15 mg/mL, aliquoted and flash-cooled in liquid nitrogen and stored at -80°C before use.

Crystals of LPHN3-OLF were made by under-oil microbatch method by mixing 1 µL of protein with an equal volume of crystallization solution containing [15-25]% polyethylene glycol 8000, [50-300] mM $MgCl_2$ and 0.1 M TAPS pH 9.0. In low $MgCl_2$ concentration (50 mM) the crystal packing was found to belong to $P6_5$ space group while high $MgCl_2$ concentration (300 mM) led to $C222_1$ crystal form. Crystals reached their full-size in one to two weeks at 20°C. The best crystals grew from proteins after spontaneous cleavage of ~5-8 kDa fragments by storing at 4°C for a few weeks. This spontaneous cleavage was verified by SDS-PAGE analysis. In contrast, freshly made proteins produced no crystals or very thin needle clusters.

Crystals of the LPHN3-OLF/FLRT3-LRR complex were made by vapor diffusion in hanging drops by mixing 1 µL of a 1:1 molar ratio mixture of the two proteins with an equal volume of crystallization solution containing 6 % polyethylene glycol 3350 and 0.2 M $NaNO_3$. Crystals reached their full-size in three to four weeks at 20°C.

For cryo-crystallography, crystals were harvested and soaked either with Paratone oil (Hampton research) or with the crystallization well solution supplemented with 20% glycerol and flash-cooled in liquid nitrogen before diffraction data collection.

Diffraction data sets were collected at Cornell High Energy Synchrotron Source (CHESS) beamline F1 (for the LPHN3-OLF high-resolution data in space group $C222_1$ and for the complex) and National Synchrotron Light Source (NSLS) beamlines X4A (for native-SAD

phasing data in space group $P6_5$) and X4C (for high-resolution data in space group $P6_5$). Complete data sets were collected from individual crystals under a cryogenic stream at 100K. The LPHN3-OLF protein contains two methionine and three cysteine residues, corresponding to an estimated Bijvoet diffraction ratio of 0.92% at an X-ray energy at 6 keV, suggesting a suitability of structure determination by native-SAD phasing. The x-ray energy of beamline X4A was thus tuned to the Cr-K edge (E = 6keV) and a helium-purged path was inserted between the crystal and the detector to reduce absorption and background. Native-SAD data sets from two $P6_5$ crystals were collected at X4A with a sample-to-detector distance of 122 mm, which limits the highest angle data to Bragg spacings of about 2.6 Å. Crystals appeared as long rods. From a single crystal, two data sets were collected, one from each of the two ends. A total of four native-SAD data sets were collected from the two $P6_5$ crystals.

All diffraction data sets were processed by XDS (Kabsch, 2010) and CCP4 program SCALA (Evans, 2011). The data reduction and analysis of two-crystal native-SAD data sets followed the established procedures as described (Liu et al., 2012; Liu et al., 2014). Briefly, four data sets from the two $P6_5$ crystals were indexed and integrated separately. After assuring the compatibility of these data sets, they were combined in POINTLESS, scaled and merged in SCALA. Bijvoet pairs were treated differently in merging. The two high-resolution native data sets were processed the same way except that Bijvoet pairs were treated the same and were merged. Data collection and reduction statistics for the three data sets are listed in Table 2.

Structure solution and refinement

The LPHN3-OLF structure - Native-SAD phasing was performed first by substructure determined with SHELXD (Sheldrick, 2010) and subsequent SAD phasing with PHENIX (Adams et al., 2011) module Phaser (Read and McCoy, 2011). For substructure determination, an Emin cutoff of 1.3 and a resolution cutoff at 2.8 were used for search of expected 5 sulfur sties by SHELXD. A total of 2,000 tries were made and the correct solution was used for further

substructure refinement and phasing in Phaser. The SAD phases were density modified by PHENIX module Resolve with a FOM of 0.293 before and 0.649 after density modification. After density modification, the experimental electron density map is of high quality and allows the automated building of 243 residues through PHENIX module AutoBuild. Further iterative model building and refinements were carried out in COOT (Emsley et al., 2010) and phenix.refine (Afonine et al., 2012), respectively. During the refinement, Bijvoet pairs were treated as different reflections. With our established f" refinement procedure (Liu et al., 2013), a structural calcium ion in the middle of the structure was identified. The refined structure was further refined against the separated collected high-resolution $P6_5$ data at 1.6 Å. To complete the high-resolution structure, additional water molecules were added and the alternative conformations were modeled to better describe the data. The high-resolution $C222_1$ structure was solved with the initial phases obtained by molecular replacement with the $P6_5$ structure as search model. Further model building and refinement were carried the same as the $P6_5$ structure. To assure the quality of the refined geometry, PROCHECK (Laskowski et al., 1993) and MolProbity (Chen et al., 2010) were used for validation of all three structures. The refinement statistics for the three structures are also listed in Table 2.

The LPHN3-OLF/FLRT3-LRR complex structure - The 3.2 Å resolution complex structure was determined using the PHENIX (Adams et al., 2011) module Phaser (Read and McCoy, 2011) with the $P6_5$ structure of LPHN3-OLF and the recently determined FLRT3-LRR structure (Seiradake et al., 2014), PDB ID: 4VDE) as search models. Iterative model building and refinements were carried out in COOT (Emsley et al., 2010) and BUSTER (Bricogne et al., 2011), respectively. During the refinement the LPHN3-OLF monomer and each repeat of FLRT3-LRR were considered as distinct TLS group. To assure the quality of the refined geometry, PROCHECK (Laskowski et al., 1993) and MolProbity (Chen et al., 2010) were used for validation of all three structures. The refinement statistics are listed in Table 2.

Structure Analysis - The structure figures were prepared using PyMOL (http://www.pymol.org/). Volume calculations of the LPHN3-OLF central pore were made with CastP (http://sts-fw.bioengr.uic.edu/castp/calculation.php). The complex interface was analyzed with PDBePISA (Krissinel and Henrick, 2007). The complex crystal packing contact analysis was performed with EPPIC (http://www.eppic-web.org/ewui/), which assigns the biological versus crystal lattice significance of protein contacts based on the number of core residues (at 95% burial), the ratio of evolutionary signal of core residues (at 70% burial) versus rim residues and a score of evolutionary signal of core residues (at 70% burial) versus random samples of other surface residues. The electrostatic surfaces were calculated with APBS (Baker et al., 2001). The conservation mapping of surface residues was carried out using the server ConSurf (Ashkenazy et al., 2010). A search of homologs of LPHN3-OLF or FLRT3-LRR was first performed using a CS-BLAST against UNIREF90. The 73 unique sequences closest to FLRT3-LRR were kept for a multiple sequence alignment (MSA) and conservation scoring. For LPHN3-OLF, the OLF domain sequences of characterized or putative of LPHNs were kept for analysis and all the other OLF domains were rejected, resulting to a MSA of 21 LPHN-OLFs, including our LPHN3-OLF.

DXMS - Comparative deuterium exchange mass spectrometry (DXMS) studies were carried out with LPHN3-OLF alone and with LPHN3-OLF/FLRT3 complex. Optimal quench condition for best sequence coverage of LPHN3-OLF was determined before performing H/D exchange experiments, as previously described (Li et al., 2011; Marsh et al., 2013). Complexes of LPHN3-OLF and FLRT3 were prepared by mixing these proteins at 1:1.2 molar ratio and incubating the mixture at 25°C for 15min, than keeping at 0°C prior to deuterium exchange. Functional hydrogen-deuterium exchange reaction of free LPHN3-OLF and LPHN3-OLF/FLRT-LRR complex were initiated by dilution of 3µl of stock solution into 9µl of D_2O buffer (8.3mM Tris pH 7.4, 150mM NaCl, pD_{READ} 7.2) and incubation at 0°C. The exchange reactions were quenched

at 10, 100, 1000, and 10000 (up to 1,000,000) sec by addition of 18µl of ice-cold 0.8% formic acid, 0.8M GuHCl, 16.6% glycerol for a final pH of 2.5. Quenched samples were then immediately frozen on dry ice and stored at -80°C before LC/MS analysis. Un-deuterated and fully deuterated control samples are also prepared as previously described (Tsalkova et al., 2012). Set of frozen samples were loaded onto a cryogenic autosampler (Woods and Hamuro, 2001) and thawed automatically at 4°C and then passed over a immobilized pepsin column for digestion of 30-40sec. Proteolytic fragments were collected on a trap column and separated using Michrom C18 reverse phase analytical column (0.2 x 50mm, 3µm) with a acetonitrile linear gradient (6.4%-38.4% over 30min). The effluent was directed into an OrbiTrap Elite Mass Spectrometer (ThermoFisher Scientific, San Jose, CA). Instruments settings were optimized to minimize the back-exchange (Walters et al., 2012). The data was acquired in either MS1 profile mode or data-dependent MS/MS mode. Peptide identification was done by the aid of Proteome Discoverer software (ThermoFisher). The centroids of the mass envelopes of deuterated peptides were calculated with DXMS Explorer (Sierra Analytics Inc., Modesto, CA) and then converted to corresponding deuterium incorporation with corrections for back-exchange (Zhang and Smith, 1993).

4- SUPPLEMENTAL REFERENCES

Adams, P.D., Afonine, P.V., Bunkoczi, G., Chen, V.B., Echols, N., Headd, J.J., Hung, L.W., Jain, S., Kapral, G.J., Grosse Kunstleve, R.W.*, et al.* (2011). The Phenix software for automated determination of macromolecular structures. Methods *55*, 94-106.

Afonine, P.V., Grosse-Kunstleve, R.W., Echols, N., Headd, J.J., Moriarty, N.W., Mustyakimov, M., Terwilliger, T.C., Urzhumtsev, A., Zwart, P.H., and Adams, P.D. (2012). Towards automated crystallographic structure refinement with phenix.refine. Acta crystallographica Section D, Biological crystallography *68*, 352-367.

Ashkenazy, H., Erez, E., Martz, E., Pupko, T., and Ben-Tal, N. (2010). ConSurf 2010: calculating evolutionary conservation in sequence and structure of proteins and nucleic acids. Nucleic acids research *38*, W529-533.

Baker, N.A., Sept, D., Joseph, S., Holst, M.J., and McCammon, J.A. (2001). Electrostatics of nanosystems: application to microtubules and the ribosome. Proc Natl Acad Sci U S A *98*, 10037-10041.

Bricogne G., Blanc E., Brandl M., Flensburg C., Keller P., Paciorek W., Roversi P, Sharff A., Smart O.S., Vonrhein C., Womack T.O. (2011). BUSTER version 2.10.2, Cambridge, United Kingdom: Global Phasing Ltd.

Brookes, E., Cao, W., and Demeler, B. (2010). A two-dimensional spectrum analysis for sedimentation velocity experiments of mixtures with heterogeneity in molecular weight and shape. European biophysics journal : EBJ *39*, 405-414.

Brookes, E., and Demeler, B. (2008). Parallel computational techniques for the analysis of sedimentation velocity experiments in UltraScan. Colloid Polym Sci *286*, 139-148.

Cao, W., and Demeler, B. (2005). Modeling analytical ultracentrifugation experiments with an adaptive space-time finite element solution of the Lamm equation. Biophysical journal *89*, 1589-1602.

Cao, W., and Demeler, B. (2008). Modeling analytical ultracentrifugation experiments with an adaptive space-time finite element solution for multicomponent reacting systems. Biophysical journal *95*, 54-65.

Chen, V.B., Arendall, W.B., 3rd, Headd, J.J., Keedy, D.A., Immormino, R.M., Kapral, G.J., Murray, L.W., Richardson, J.S., and Richardson, D.C. (2010). MolProbity: all-atom structure validation for macromolecular crystallography. Acta crystallographica Section D, Biological crystallography *66*, 12-21.

Comoletti, D., Flynn, R., Jennings, L.L., Chubykin, A., Matsumura, T., Hasegawa, H., Sudhof, T.C., and Taylor, P. (2003). Characterization of the interaction of a recombinant soluble neuroligin-1 with neurexin-1 beta. J Biol Chem *278*, 50497-50505.

Demeler, B. (2010). Methods for the design and analysis of sedimentation velocity and sedimentation equilibrium experiments with proteins. Current protocols in protein science / editorial board, John E Coligan [et al] Chapter 7, Unit 7 13.

Demeler, B., and van Holde, K.E. (2004). Sedimentation velocity analysis of highly heterogeneous systems. Analytical biochemistry *335*, 279-288.

Duarte, J.M., Srebniak, A., Scharer, M.A., and Capitani, G. (2012). Protein interface classification by evolutionary analysis. BMC bioinformatics *13*, 334.

Emsley, P., Lohkamp, B., Scott, W.G., and Cowtan, K. (2010). Features and development of Coot. Acta crystallographica Section D, Biological crystallography *66*, 486-501.

Evans, P.R. (2011). An introduction to data reduction: space-group determination, scaling and intensity statistics. Acta crystallographica Section D, Biological crystallography *67*, 282-292.

Gorbet, G., Devlin, T., Hernandez Uribe, B.I., Demeler, A.K., Lindsey, Z.L., Ganji, S., Breton, S., Weise-Cross, L., Lafer, E.M., Brookes, E.H.*, et al.* (2014). A parametrically constrained optimization method for fitting sedimentation velocity experiments. Biophysical journal *106*, 1741-1750.

Kabsch, W. (2010). Xds. Acta crystallographica Section D, Biological crystallography *66*, 125-132.

Krissinel, E., and Henrick, K. (2007). Inference of macromolecular assemblies from crystalline state. Journal of molecular biology *372*, 774-797.

Laue, T.M., Shah, B.D., Ridgeway, T.M., Pelletier, S.L. (1992).Computer-aided interpretation of analytical sedimentation data for proteins.In Analytical Ultracentrifugation in Biochemistry and Polymer Science,(Edt. S. E. Harding, A. J. Rowe, and J. C. Horton.Cambridge, Royal Society of Chemistry),p90-125.

Laskowski, R.A., Moss, D.S., and Thornton, J.M. (1993). Main-chain bond lengths and bond angles in protein structures. Journal of molecular biology *231*, 1049-1067.

Li, S., Tsalkova, T., White, M.A., Mei, F.C., Liu, T., Wang, D., Woods, V.L., Jr., and Cheng, X. (2011). Mechanism of intracellular cAMP sensor Epac2 activation: cAMP-induced conformational changes identified by amide hydrogen/deuterium exchange mass spectrometry (DXMS). J Biol Chem *286*, 17889-17897.

Liu, Q., Dahmane, T., Zhang, Z., Assur, Z., Brasch, J., Shapiro, L., Mancia, F., and Hendrickson, W.A. (2012). Structures from anomalous diffraction of native biological macromolecules. Science *336*, 1033-1037.

Liu, Q., Guo, Y., Chang, Y., Cai, Z., Assur, Z., Mancia, F., Greene, M.I., and Hendrickson, W.A. (2014). Multi-crystal native SAD analysis at 6 keV. Acta crystallographica Section D, Biological crystallography *70*, 2544-2557.

Liu, Q., Liu, Q., and Hendrickson, W.A. (2013). Robust structural analysis of native biological macromolecules from multi-crystal anomalous diffraction data. Acta crystallographica Section D, Biological crystallography *69*, 1314-1332.

Marsh, J.J., Guan, H.S., Li, S., Chiles, P.G., Tran, D., and Morris, T.A. (2013). Structural insights into fibrinogen dynamics using amide hydrogen/deuterium exchange mass spectrometry. Biochemistry *52*, 5491-5502.

O'Sullivan, M.L., de Wit, J., Savas, J.N., Comoletti, D., Otto-Hitt, S., Yates, J.R., and Ghosh, A. (2012). FLRT Proteins Are Endogenous Latrophilin Ligands and Regulate Excitatory Synapse Development. Neuron *73*, 903-910.

Read, R.J., and McCoy, A.J. (2011). Using SAD data in Phaser. Acta crystallographica Section D, Biological crystallography *67*, 338-344.

Reeves, P.J., Callewaert, N., Contreras, R., and Khorana, H.G. (2002). Structure and function in rhodopsin: High-level expression of rhodopsin with restricted and homogeneous N-glycosylation by a tetracycline-inducible N-acetylglucosaminyltransferase I-negative HEK293S stable mammalian cell line. P Natl Acad Sci USA *99*, 13419-13424.

Schuck, P., and Demeler, B. (1999). Direct sedimentation analysis of interference optical data in analytical ultracentrifugation. Biophysical journal *76*, 2288-2296.

Seiradake, E., del Toro, D., Nagel, D., Cop, F., Hartl, R., Ruff, T., Seyit-Bremer, G., Harlos, K., Border, E.C., Acker-Palmer, A.*, et al.* (2014). FLRT structure: balancing repulsion and cell adhesion in cortical and vascular development. Neuron *84*, 370-385.

Sheldrick, G.M. (2010). Experimental phasing with SHELXC/D/E: combining chain tracing with density modification. Acta crystallographica Section D, Biological crystallography *66*, 479-485.

Tsalkova, T., Mei, F.C., Li, S., Chepurny, O.G., Leech, C.A., Liu, T., Holz, G.G., Woods, V.L., Jr., and Cheng, X. (2012). Isoform-specific antagonists of exchange proteins directly activated by cAMP. Proc Natl Acad Sci U S A *109*, 18613-18618.

Walters, B.T., Ricciuti, A., Mayne, L., and Englander, S.W. (2012). Minimizing back exchange in the hydrogen exchange-mass spectrometry experiment. Journal of the American Society for Mass Spectrometry *23*, 2132-2139.

Woods, V.L., Jr., and Hamuro, Y. (2001). High resolution, high-throughput amide deuterium exchange-mass spectrometry (DXMS) determination of protein binding site structure and dynamics: utility in pharmaceutical design. Journal of cellular biochemistry Supplement *Suppl 37*, 89-98.

Zhang, Z., and Smith, D.L. (1993). Determination of amide hydrogen exchange by mass spectrometry: a new tool for protein structure elucidation. Protein science : a publication of the Protein Society *2*, 522-531.